JOURNAL OF SPACECRAFT AND ROCKETS
Vol. 37, No. 5, September–October 2000

Numerical Investigation of Supersonic Jet Interaction for Axisymmetric Bodies

Mary Jane Graham*
U.S. Military Academy, West Point, New York 10996-1786
and
Paul Weinacht†
U.S. Army Research Laboratory, Aberdeen Proving Ground, Maryland 21005-5066

A detailed numerical investigation of the interaction between a lateral jet and the external flow has been performed for several axisymmetric bodies. Numerical predictions of the supersonic viscous flow has been obtained using an existing Reynolds-averaged Navier–Stokes computational technique. The computational results have been validated using surface pressure and global force and moment measurements from a previously published experimental investigation. Surface-pressure measurements on the body are generally in good agreement with the experimental measurements, particularly in the region downstream of the side jet. Force and moment predictions also show excellent agreement with experimental measurements. The results show that the interaction of the jet with the external flow produces a complex flowfield that may be difficult to characterize using simpler approaches. The effects of nose shape, angle of attack, mass flow, and flight velocity have been investigated. For the geometries and flight conditions considered here, flight velocity and jet mass flow appear to have the most significant effect on the force and moments, whereas nose shape and small variations in angle of attack produced relatively small effects. These conclusions are supported by the results obtained in the prior experimental investigation.

Nomenclature

A_e	=	jet-exit area
a_∞	=	freestream speed of sound
$C_{m_{ji}}$	=	jet-interaction moment coefficient
C_N	=	normal force coefficient
C_{N_j}	=	jet force coefficient
$C_{N_{ji}}$	=	jet-interaction force coefficient
D	=	projectile diameter
$\hat{E}, \hat{F}, \hat{G}$	=	flux vectors in transformed coordinates
e	=	total energy per unit volume
J	=	Jacobian
K	=	jet-interaction amplification factor
L	=	body length
M	=	freestream Mach number
$\dot{m}$	=	jet mass-flow rate
p	=	pressure
Re	=	Reynolds number, $a_\infty \rho_\infty D/\mu_\infty$
$\hat{S}$	=	viscous flux vector
S_{ref}	=	reference area of projectile, $\pi D^2/4$
t	=	time
u, v, w	=	velocity components in x, y, z directions
u_e	=	jet-exit velocity
V_∞	=	freestream velocity
x, y, z	=	axial, horizontal, and vertical coordinates
α	=	angle of attack
γ	=	ratio of specific heats
μ	=	viscosity
ξ, η, ζ	=	transformed coordinates in Navier–Stokes equations
ρ	=	density
ϕ	=	circumferential coordinate, measured from vertical axis

Subscript

∞	=	denotes freestream conditions

Received 31 March 1999; revision received 1 March 2000; accepted for publication 16 March 2000.

*Assistant Professor. Member AIAA.
†Aerospace Engineer. Associate Fellow AIAA.

Introduction

THERE are many approaches for affecting or controlling the maneuver of a flight vehicle. These include the use of deflecting fins or canards as well as the use of lateral control jets. The lateral jet control of a missile provides advantages over conventional control surfaces in that the external aerodynamics of the flight vehicle are unaffected except during the controlled portion of the flight. However, the flowfield that results from the interaction between a gaseous jet and a supersonic external flow is complicated. The purpose of the current research is to develop a computational capability to assess the performance of control jets and to obtain a quantitative understanding of the flow phenomena produced by control jets.

The flowfield that results from the interaction of a side (lateral) jet injection into a supersonic external flow, called the jet-interaction flowfield, has been the subject of several experimental[1–5] and numerical[6–10] investigations. The typical jet-interaction flowfield is complicated because of the jet's interruption of the oncoming external flow. The qualitative features of the jet-interaction flowfield include regions of shock/boundary-layer interaction and flow separation that have an effect on the large regions of the flowfield around the body. Figure 1 shows a schematic diagram of the flow topology caused by a lateral jet.

As is the case with jet-off supersonic flow, a body bow shock is formed at the nose tip of the projectile. Further downstream from the nose, the emission of the jet creates a blocking effect to the oncoming flow in the vicinity of the jet producing boundary-layer separation and recirculation upstream of the jet. The upstream boundary-layer separation contains two counter-rotating recirculation regions. The first is located directly upstream of the jet and moves in a counterclockwise direction, as it is reinforced by the outflow from the jet. The second is directly upstream of the first and moves in a clockwise direction as it interacts with the oncoming flow and the first recirculation region.

Figure 2 shows velocity particle traces showing the described recirculation region. This separation region upstream of the jet sets up a wedge-shaped (or ramped) area, which has the effect of deflecting the flow laterally around the body so that a region of high pressure is felt under the projectile. The details of the upstream interaction are important because it is along the upper part of this region that the separation shock forms. Because the jet stream acts as an obstacle to the external flow, another shock wave originates directly upstream of the jet and above the separation region called the jet

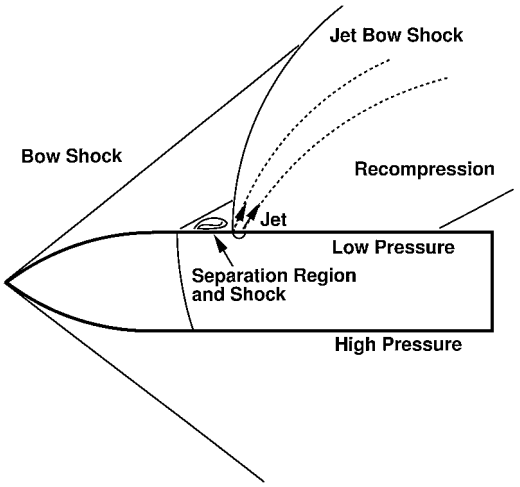

Fig. 1 Schematic of jet-interaction flowfield.

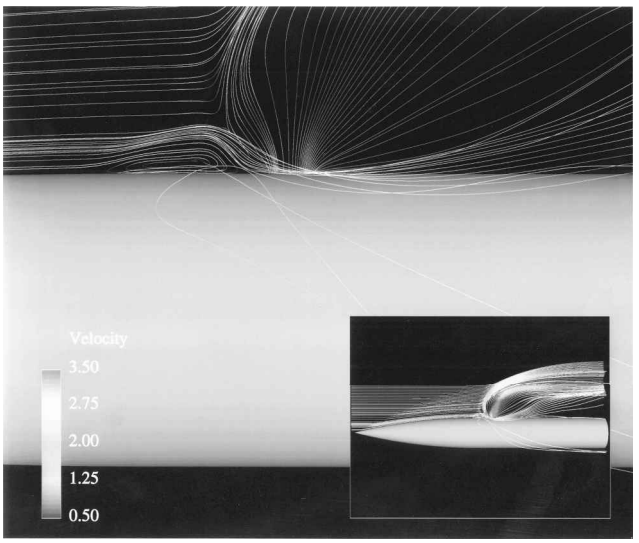

Fig. 2 Particle traces from computed flowfield.

bow shock. The jet bow shock moves outward from the body and bends backward as the jet flow is deflected by the external flow. A strong turbulent wake results from the jet flowfield interactions and extends over a significant portion of the projectile body. Eventually, a recompression shock forms in the wake downstream of the jet. The jet bow shock also moves laterally around the jet, the effects of which are felt on the underbody of the projectile. Figure 3 is the velocity contours for a sharp-nose projectile at Mach 3.3 and zero degrees angle of attack (AOA). The regions of low velocity (and high pressure) under the projectile show the visible effect of the jet bow shock as it wraps around the body.

The presence of a lateral jet has a significant effect on the entire flowfield. The complex pressure distribution induced by the jet interaction can lead to an increase or a decrease in the control force. The fact that the bow shock has a tendency to wrap around the body and produce a high-pressure region on the underside can reduce the effectiveness of the lateral jet. The resulting disturbances caused by the jet interaction alter the forces and moments compared to those that the thrust of the jet alone would be expected to produce.

In the current study a numerical approach has been applied to investigate the jet-interaction phenomena for axisymmetric bodies with a single lateral jet in supersonic flight. An overset grid approach has been applied to more easily resolve the geometry and flow physics associated with the jet-interaction problem. Most of the previous numerical studies approximated the nozzle geometry so that it would conform to the computational mesh. The overset grid approach eliminates this approximation. The current study presents both detailed pressure comparisons and global force and moment

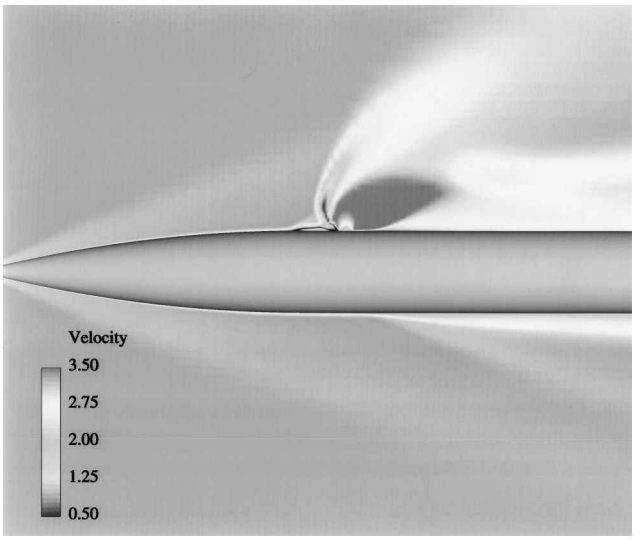

Fig. 3 Velocity contours from computed flowfield.

comparisons as a means of validating the computational approach. The numerical results are validated with both detailed pressure and global force and moment measurements from an extensive study by Brandeis and Gill[1,2] and provide additional insight into their experimental results. Many of the previous numerical investigations focused on either pressure or global force and moment comparisons. The current study provides both types of comparisons. The pressure comparisons focus on the regions of the body most affected by the jet-interaction phenomenon both upstream and downstream of the jet. The pressure results provide important details about the flowfield that are useful in interpreting the global force and moment comparisons. In general, the comparisons between the predicted pressure and global force and moments are in good agreement.

Computational Technique

Governing Equations

The nonreacting compressible Newtonian viscous flow about a flight vehicle is governed by the equations of mass, momentum, and energy conservation: the Navier–Stokes equations. For these computations the complete set of three-dimensional, time-dependent, generalized-geometry, Reynolds-averaged, thin-layer, Navier–Stokes equations for generalized coordinates ξ, η, and ζ are used and can be written as follows[10]:

$$\frac{\partial \hat{q}}{\partial t} + \frac{\partial \hat{E}}{\partial \xi} + \frac{\partial \hat{F}}{\partial \eta} + \frac{\partial \hat{G}}{\partial \zeta} = \frac{1}{Re}\frac{\partial \hat{S}}{\partial \zeta} \tag{1}$$

$\xi = \xi(x, y, z, t)$, $\eta = \eta(x, y, z, t)$, and $\zeta = \zeta(x, y, z, t)$ are the longitudinal coordinate (direction along the body), the circumferential coordinate (direction around the body), and the nearly normal coordinate (outward direction from the body surface), respectively.

The inviscid flux vectors $\hat{E}$, $\hat{F}$, and $\hat{G}$ and the viscous term $\hat{S}$ are functions of the dependent variable $q^T = (\rho, \rho u, \rho v, \rho w, e)$. The inviscid flux vectors and the source term are shown as follows. Details of the thin-layer viscous term are available in the literature:

$$\hat{E} = \frac{1}{J}\begin{bmatrix} \rho U \\ \rho u U + \xi_x p \\ \rho v U + \xi_y p \\ \rho w U + \xi_z p \\ (e + p)U \end{bmatrix}, \qquad \hat{F} = \frac{1}{J}\begin{bmatrix} \rho V \\ \rho u V + \eta_x p \\ \rho v V + \eta_y p \\ \rho w V + \eta_z p \\ (e + p)V \end{bmatrix}$$

$$\hat{G} = \frac{1}{J}\begin{bmatrix} \rho W \\ \rho u W + \zeta_x p \\ \rho v W + \zeta_y p \\ \rho w W + \zeta_z p \\ (e + p)W \end{bmatrix} \tag{2}$$

The contravariant velocity components (in the ξ, η, and ζ directions) that appear in the inviscid flux terms have the following form:

$$U = u\xi_x + v\xi_y + w\xi_z \tag{3}$$

$$V = u\eta_x + v\eta_y + w\eta_z \tag{4}$$

$$W = u\zeta_x + v\zeta_y + w\zeta_z \tag{5}$$

The Cartesian velocity components (u, v, w) are retained as the dependent variables and are nondimensionalized with the respect to a_∞ (the freestream speed of sound). The local pressure is determined using an appropriate equation of state (i.e., the pressure is related to the dependent variables by applying the ideal gas law):

$$p = (\gamma - 1)[e - 0.5\rho(u^2 + v^2 + w^2)] \tag{6}$$

Density ρ is referenced to ρ_∞ and the total energy e to $\rho_\infty a_\infty^2$.

The form of the mass-averaged Navier–Stokes equations requires a model for the turbulent eddy viscosity. There are numerous approaches for determining the turbulent viscosity. The turbulent contributions are supplied through the algebraic two-layer eddy viscosity model developed by Baldwin and Lomax,[11] which is patterned after the model of Cebeci.[12]

Numerical Technique

The time-dependent Navier–Stokes equations are solved using an time-iterative solution technique to obtain the final steady-state converged solution. The particular time-marching technique applied here is the implicit, partially flux-split, upwind numerical scheme developed by Ying et al.[13] and Sahu and Steger[14] and is based on the flux-splitting approach of Steger and Warming.[15] In its original form the technique was referred to as the F3D technique. This scheme uses central differencing in the normal and circumferential direction η and ζ, respectively, and flux splitting in the streamwise direction ξ. Rather than directly invert the implicit equation, a two-factor implicit technique similar to that of Steger and Buning[16] is used. The resulting factored implicit equation is shown as follows:

$$\left[I + i_b h\delta_\xi^b(\hat{A}^+)^n + i_b h\delta_\zeta\hat{C}^n - i_b h(1/Re)\,\bar{\delta}_\zeta(1/J)\hat{M}^n J - i_b D_i|_\zeta\right]q^* = \text{RHS} \tag{7}$$

$$\left[I + i_b h\delta_\xi^f(\hat{A}^-)^n + i_b h\delta_\eta\hat{B}^n - i_b D_i|_\eta\right]\Delta\hat{q}^n = q^* \tag{8}$$

$$\text{RHS} = -i_b\Delta t\left[\delta_\xi^b(\hat{E}^+)^n + \delta_\xi^f(\hat{E}^-)^n + \delta_\eta\hat{F}^n + \delta_\zeta\hat{G}^n - (1/Re)\,\bar{\delta}\hat{S}^n - D_e\hat{q}^n\right] \tag{9}$$

where $h = \Delta t$. Here, δ is typically a three-point, second-order accurate central difference operator, $\bar{\delta}$ is a midpoint operator used with the viscous terms, and the operators δ_ξ^f and δ_ζ^b are the forward and backward, respectively, three-point difference operators. The Jacobian matrices $\hat{A}$, $\hat{B}$, $\hat{C}$, and $\hat{M}$ result from local linearization of the fluxes about the previous time level[17] [e.g., $\hat{E}^{n+1} = \hat{E}^n + \hat{A}^n(\hat{q}^{n+1} - \hat{q}^n) + \mathcal{O}(\Delta t^2)$, where $\hat{A} = \partial\hat{E}/\partial\hat{q}$].

The two-factor implicit algorithm involves two sweeps through the grid at each time step. The first sweep involves inverting the block tridiagonal system of equations shown in Eq. (7) along constant η grid lines to determine the intermediate solution variable q^*. During the second sweep, a second block tridiagonal system of equations [Eq. (8)] is inverted along grid lines of constant ζ to determine the dependent variable $\Delta\hat{q}^n$. The two-factor implicit algorithm reduces the computational requirements of the approach compared with the three-factor, central-difference, implicit algorithm of Beam and Warming.[17]

The algorithm contains additional numerical smoothing terms $D_i|_\eta$, $D_i|_\zeta$, and D_e to suppress numerical oscillations associated with the odd-even decoupling produced by the central differencing in the η and ζ directions.[12]

Chimera Composite Overset Structured Grids

To more easily model the geometry and resolve the flow physics associated with the lateral jet problem, the chimera composite overset grid technique has been applied. The chimera technique is a domain decomposition approach that allows the entire flowfield to be meshed into a collection of independent grids, where each piece is gridded separately and overset into a main grid. In current computations the flight body with lateral jet was subdivided into three distinct grids: one for the body, one adjacent to the jet, and one for the jet nozzle. Overset grids are not required to join in any special way. Usually there is a major grid that covers the main domain (the external flowfield about the projectile), and minor grids are generated to resolve the rest of the body or sections of the body (the jet and the nozzle regions).

Figure 4 displays the computational mesh, showing the main grid for the projectile body along with an overset grid to better capture the physics of the jet interaction with the external flow. The overset jet grid is seen here residing on top of the jet exit as a cylinder with a radius larger than the jet hole itself. A third grid, used to model the jet nozzle, resides underneath the jet grid. The communication between the nozzle grid and the jet grid, however, is point-to-point zonal. Figure 5 is a close-up of the grid near the jet hole, which is covered by the nozzle grid and jet grid. It also shows the chimera grid for the jet and the projectile body. A hole has been cut into the projectile grid by the scheme. Because each component grid is generated independently, portions of one grid may be found to lie within the solid boundary contained in another grid. Such points lie outside the computational domain and are excluded from the solution

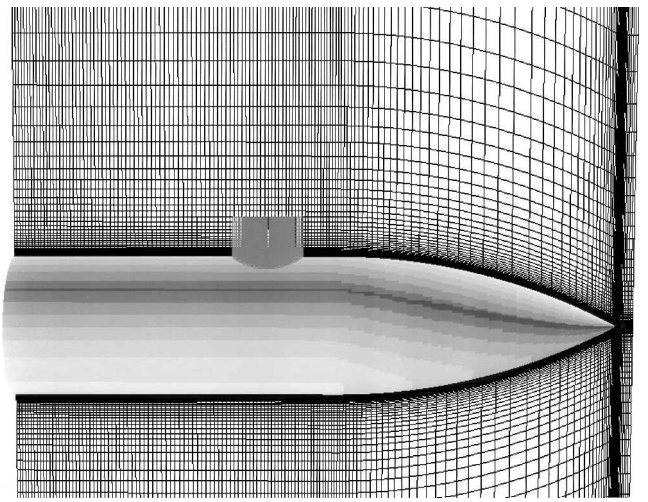

Fig. 4 Computational mesh.

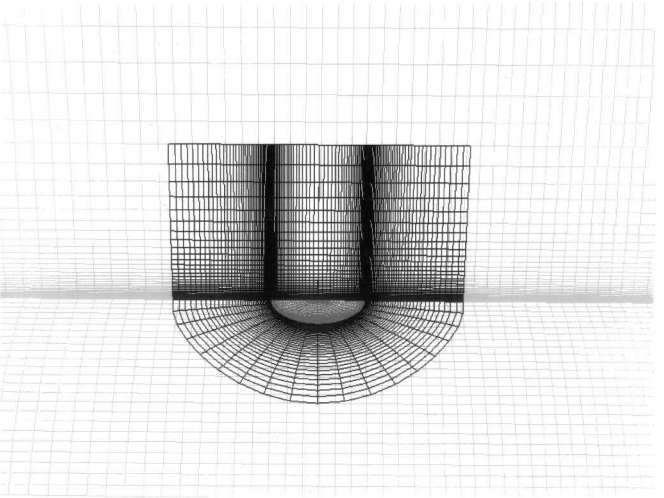

Fig. 5 Chimera gridding near jet nozzle.

process. Any viable structured grid flow solver can be adapted to work within the framework of the chimera scheme.

The thin-layer Navier–Stokes equations, shown in Eq. (7), have been modified for the chimera scheme.[18] The single and overset grid versions of the algorithm are identical except for the variable i_b, which accommodates the possibility of having arbitrary holes in the grid. The array i_b has the values of either 0 (for hole points) or 1 (for conventional field points-mesh point within the computational domain updated by the flow solver or boundary conditions). Thus, points inside a hole are not updated (i.e., $\Delta\hat{q}^n = 0$), and the solution values on intergrid boundary points are supplied via interpolation from corresponding solutions in the overlap region of neighboring grid systems.[19]

Grid Refinement and Computational Time

The baseline computational grid used to generate the published results consisted of approximately 1.1 million points; 153 ×93 ×70 for the projectile (background) grid in the longitudinal, circumferential, and normal directions, respectively; 65 ×21 ×50 for the cylindrically shaped jet grid in the radial, circumferential, and normal directions, respectively; 25 ×21 ×21 for the nozzle grid in the radial, circumferential, and normal directions. The computational mesh employed a mirror plane of symmetry in the circumferential direction. A grid refinement study was performed to assess grid convergence for the baseline computational grid. Coarse grid solutions were obtained using 113 ×70 ×53, 49 ×16 ×38, and 19 ×16 ×16 grids for the projectile, jet, and nozzle meshes. Fine grid solutions were obtained using 193 ×116 ×88, 81 ×28 ×63, and 31 ×26 ×26 grids for the projectile, jet, and nozzle meshes. The dimensions given represent a 25% decrease or increase, respectively, in each direction for fine and coarse grids, resulting in approximately a halving and doubling of the total number of grid points compared with the baseline grid.

The fine and coarse grid solutions were interpolated back onto the baseline grid, and comparisons were made of the circumferential pressure distribution at the axial stations where experimental data were available. There is an average difference of less than 2.1% between the fine and baseline grid solutions. The same interpolation was made for the coarse and baseline grid. In the vicinity of the jet, there is as much as an 11% difference between the two results. Downstream of the jet, however, an average of less than 3% was observed. Comparisons of the computed global jet-interaction force coefficients for the coarse and fine grids were within 5% of the results obtained on the baseline grid.

A complete simulation on the baseline grid took approximately 250 CPU hours on an SGI Origin 2000. The solutions were run in parallel using eight processors, and a parallel speed up of 5.4 was obtained.

Results

Validation of the computational approach for the jet-interaction problem was accomplished by comparing the predictions with data from a previously published wind-tunnel investigation.[1] Supplemental experimental results for the validation were provided courtesy of RAFAEL, Ministry of Defense Directorate of Defense Research and Development.[1] The experiments were carried out at several different wind-tunnel sites (Technion and Israel Aircraft Industries supersonic tunnels) to span the flight regime from Mach 2 to 10. Although the experimental investigation was quite extensive in scope, the current computational study focused on normal jet injection from a single nozzle geometry at Mach 2 and 3.3. The Reynolds numbers based on diameter are 2.32×10^6 and 4.13×10^6, respectively. The static temperatures are 155 and 84.2 deg K, respectively. Four different bodies geometries were examined in the study. Surface-pressure and global force comparisons were made to validate the computational approach.

Figure 6 shows four body geometries addressed in this study. The reference diameter of each of the models was 50 mm. For all four geometries the jet nozzle was located 0.5 calibers downstream of the ogive-cylinder junction. A single 8-mm circular nozzle that was designed to achieve sonic flow at the exit was examined here, although additional geometries were considered in the experiment.

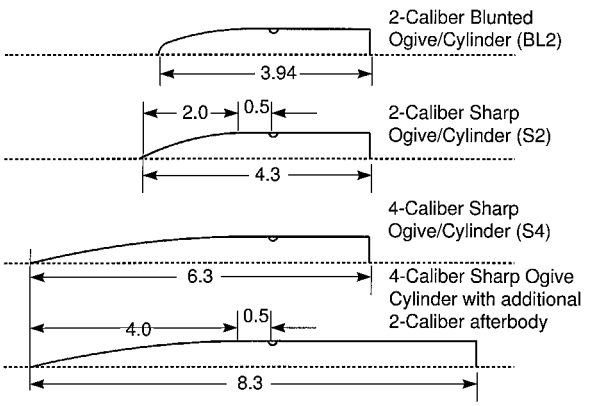

Fig. 6 Schematic of body geometries.

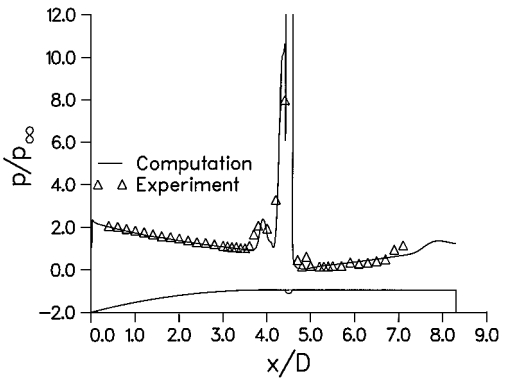

Fig. 7 Longitudinal pressure distribution: jet plane, $M = 3.33$, $\dot{m}$ = 0.54 kg/s.

Each of the first three bodies had a 2.3-caliber cylindrical afterbody with three different nose shapes: a 2-caliber ogive with a spherically blunted tip (bluntness ratio of 0.5), a sharp-tipped 2-caliber ogive, and a sharp-tipped 4-caliber ogive. Additional testing of the sharp-tipped 4-caliber ogive configuration was performed with 1 caliber of afterbody removed. Global force and moment wind-tunnel tests were performed on these bodies. The fourth body geometry was identical to the sharp-tipped 4-caliber ogive configuration, except that it had an additional 2 calibers of cylindrical afterbody. This model was used for surface-pressure measurements.

Aerodynamic Pressure Predictions

In the experimental study pressure data were taken for the 4-caliber sharp-tipped ogive shown at the bottom of Fig. 6, with a total of about 100 pressure taps being used over the body. No force or moment data were recorded during the pressure survey. Computational results were obtained at Mach 3.33 and $\alpha = 0$ deg at the wind-tunnel Reynolds number and static temperature. The jet mass-flow rates of 0.54 and 0.36 kg/s were considered. The experimental and computational longitudinal pressure distributions along the jet plane are shown in Figs.7 and 8 for the mass-flow rates of 0.54 and 0.36 kg/s, respectively. Along the forward 3.5 calibers of the ogive, the pressure distribution is essentially identical to the jet-off pressure distribution, which shows a decreasing trend as the body slope decreases. The pressure increase at $x/D = 3.7$ is directly associated with the separation region caused by the jet emission. As already stated, the jet causes an upstream, wedgelike separation region, which acts as a ramp to the flowfield. An oblique shock is formed, accounting for the pressure increase at $x/D = 3.7$. The pressure then decreases slightly over the recirculation region and jumps up dramatically, as expected, in the presence of the jet ($x/D \approx 4.3$). Downstream of the jet is a sharp decrease in the pressure. This feature is expected because a vacuum-like region forms downstream of the jet. The pressure remains low at $x/D = 4.8$ and increases slightly through $x/D = 6.8$, where one sees a more marked increase in the pressure because of the recompression shock. The

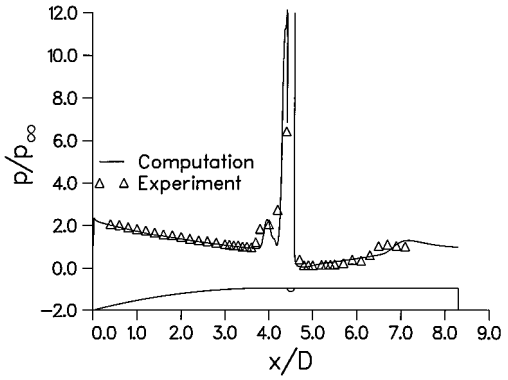

Fig. 8 Longitudinal pressure distribution: jet plane, $M = 3.33$, $\dot{m} = 0.36$ kg/s.

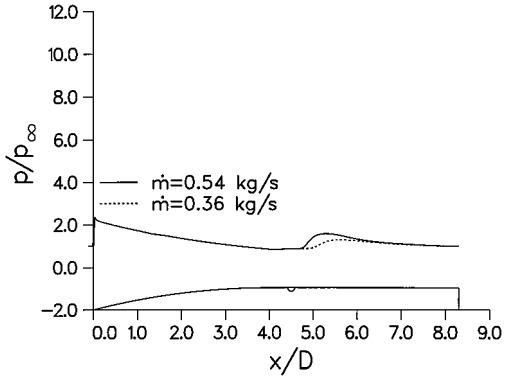

Fig. 9 Longitudinal pressure distribution: $\phi = 180$ deg $M = 3.33$, $\dot{m} = 0.36$ and 0.54 kg/s.

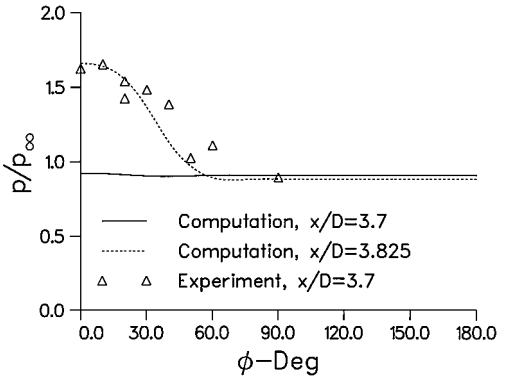

Fig. 10 Circumferential pressure distribution: $x/D = 3.7$, $M = 3.33$, $\dot{m} = 0.54$ kg/s.

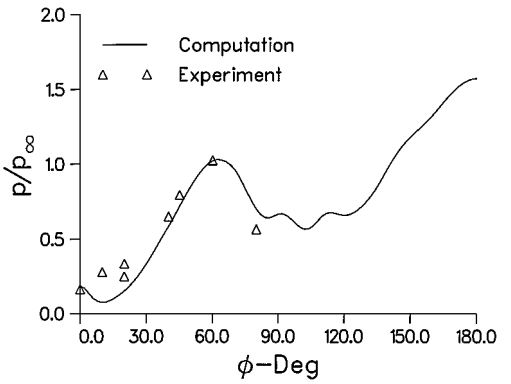

Fig. 11 Circumferential pressure distribution: $x/D = 5.3$, $M = 3.33$, $\dot{m} = 0.54$ kg/s.

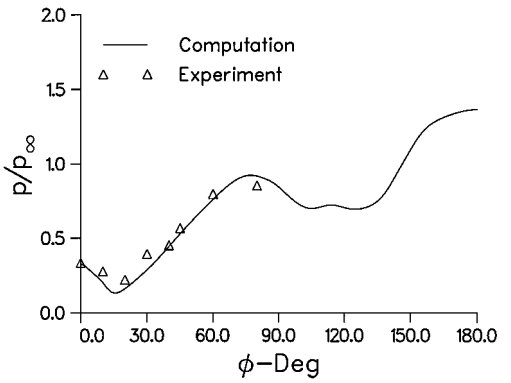

Fig. 12 Circumferential pressure distribution: $x/D = 5.9$, $M = 3.33$, $\dot{m} = 0.54$ kg/s.

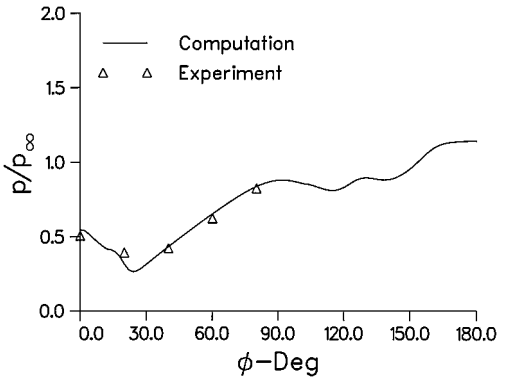

Fig. 13 Circumferential pressure distribution: $x/D = 6.7$, $M = 3.33$, $\dot{m} = 0.54$ kg/s.

results are qualitatively the same for the mass-flow rate 0.36 kg/s. The most significant difference in the pressure distributions occur at the aft end of the body and are associated with the forward movement of the recompression shock for the lower mass-flow rate. The results obtained are in very good agreement with those obtained by Brandeis and Gill.[1]

The strong interaction produced by the jet influences the circumferential pressure distribution on the body. Figure 9 shows the longitudinal pressure 180 deg from the jet plane for both mass-flow rates. Note the marked increase in pressure at $x/D = 4.7$. The increase is because the shock formation upstream of the jet moves laterally around the body and wraps around to produce an interaction underneath the projectile. The pressure distributions for both mass-flow rates are similar although the higher mass-flow rate appears to produce a higher pressure over the forward part of the interaction region. The combination of the low pressure aft of the jet along the jet plane and the high pressure on the opposite side of the body results in a force that opposes the thrust produced by the jet.

Figures 10–13 show the circumferential pressure distribution at various axial locations for ϕ ranging from 0 deg (jet plane) to 180 deg for Mach 3.33 and a mass-flow rate 0.54 kg/s. Figure 10 shows the predicted and measured pressure distributions in front of the jet at $x/D = 3.7$. As noted in Fig. 7, the computed pressure distribution shows that the interaction region occurs slightly farther downstream than in the experiment. To obtain good agreement with experiment, computed circumferential pressure data at $x/D = 3.825$ were extracted. This feature can be seen in Fig. 7, where the initial increase in pressure in the computational results occurs slightly farther down from the experiment. This slight disagreement may be a result of turbulence modeling issues and is a subject of future investigation. Within the interaction region the pressure is higher at $\phi = 0$ deg and decreases with circumferential angle until about $\phi = 90$ deg, where the influence of the jet is no longer felt on this part of the body.

Figures 11–13 show the circumferential pressure distributions downstream of the jet at the axial locations $x/D = 5.3$, 5.9, and 6.7. In general, the circumferential pressure distributions show lower

pressures in the jet plane and higher pressures on the opposite side of the body. The lower pressure seen in these graphs is caused by the vacuumlike region that forms downstream of the jet. The predicted pressure distributions are in good agreement with the experimental measurements. The predicted flowfield results indicate that the pressure minimum in the circumferential pressure distributions downstream of the jet is associated with a crossflow vortex that exists between the symmetry plane and the pressure minimum. The good correlation between the experimentally determined location of the pressure minimum and prediction appears to exist.

The circumferential pressure distributions for the mass-flow rate of 0.36 kg/s are similar to the 0.54 kg/s mass-flow case. In front of the jet, the computed pressure distributions indicated that the computed recirculation region was located downstream of the location indicated in the experiment. As shown in Figs. 14–16, good agreement between computation and experiment was found downstream of the jet. The pressure distributions show only small differences between the two mass-flow cases with the most significant differences found on the side of the body opposite the jet.

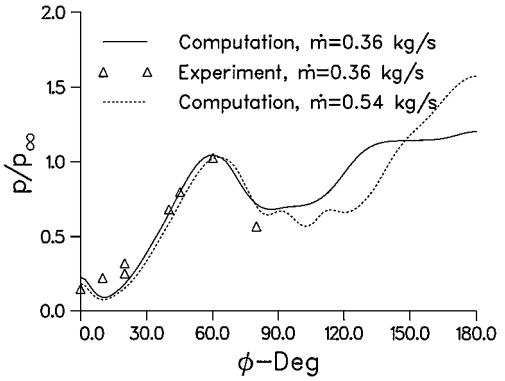

Fig. 14 Circumferential pressure distribution: $x/D = 5.3$, $M = 3.33$, $\dot{m} = 0.36$ and 0.54 kg/s.

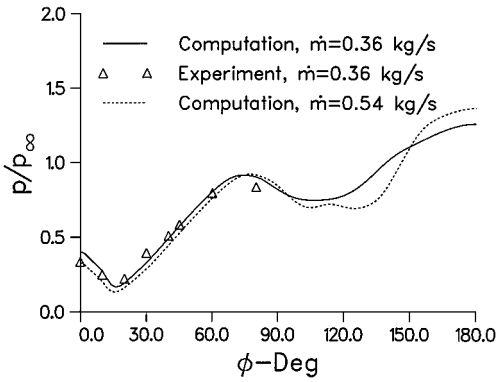

Fig. 15 Circumferential pressure distribution: $x/D = 5.9$, $M = 3.33$, $\dot{m} = 0.36$ and 0.54 kg/s.

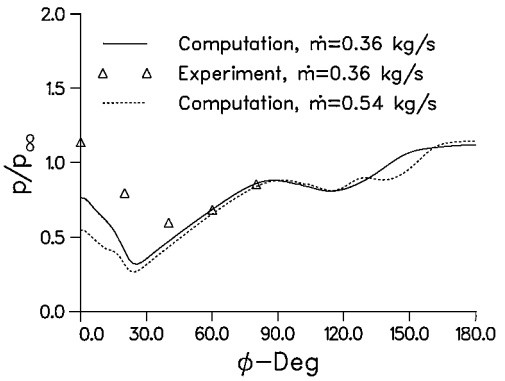

Fig. 16 Circumferential pressure distribution: $x/D = 6.7$, $M = 3.33$, $\dot{m} = 0.36$ and 0.54 kg/s.

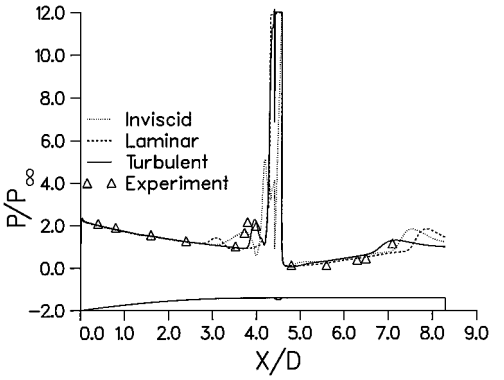

Fig. 17 Comparison of longitudinal pressure distributions for the laminar, inviscid, turbulent, and experiment cases: jet plane, AOA = 0, $M = 3.33$.

The pressure predictions reported have been performed using the Baldwin/Lomax turbulence model, as described in an earlier section. Computations were also performed for laminar and inviscid cases. Figure 17 shows a comparison of the longitudinal pressure distribution for the laminar, inviscid, and turbulent predictions with the experimental results. In both the laminar and the inviscid cases, the details of the separation region and recompression shock region are different in both the magnitude of the pressure and the axial location of the regions. For both the laminar and inviscid predictions the separation region in front of the jet extends farther forward and has a lower peak pressure than the turbulent predictions and experimental measurements. The predicted recompression region behind the jet is located farther downstream and has a higher peak pressure than in the turbulent and experimental results. In addition, the jet-interaction force amplification factor obtained from the laminar and inviscid cases underpredict the wind-tunnel measurement by 10%, whereas turbulent prediction is within 3% of the measurement. These results indicate the relative importance of the viscous effects for the jet-interaction problem.

Aerodynamic Force Predictions

For the jet-interaction problem the total force acting on the body can be decomposed into three components: the aerodynamic force on the external body in the absence of the jet, the force produced at the jet exit, and the aerodynamic interaction force produced by the jet with the external flowfield. In the current paper the aerodynamic force on the external body is typically produced when the body is at an AOA with the freestream flow. The force produced at the jet exit results from a combination of the momentum flux through the jet nozzle and the integrated pressure at the jet exit. Given that the exit conditions for the jet are fixed as a boundary condition for the computations, this force component can be explicitly calculated prior to the flowfield computation. The third force component accounts for the force produced by the interaction of the jet with external flowfield.

The relationship of these three force components to the total force F can be described by the following equation, where $F_{\text{no-jet}}$ is the force in the absence of the jet, F_j is the force produced at the jet exit, and F_{ji} is the jet-interaction force:

$$F = F_{\text{no-jet}} - (F_j + F_{\text{ji}}) \tag{10}$$

The negative sign associated with the two jet forces results because the jet-exit hole is located on the upper surface of the body in the current study and produces a downward force when activated. The jet-off force component typically produces an upward force for positive AOA. A positive value of F_{ji} indicates that the interaction force produces an effect that augments the jet force F_j, whereas a negative value of F_{ji} indicates a reduction in the total force produced by the jet. The jet-interaction force accounts for the complete interaction produced by the jet with the external flowfield and can vary with AOA and jet mass-flow rate.

Typically, the force is expressed in nondimensional coefficient form as shown in the following:

$$C_N = F \Big/ \tfrac{1}{2}\rho_\infty V_\infty^2 S_{\text{ref}} \tag{11}$$

$$C_N = C_{N_{\text{no-jet}}} - \left(C_{N_j} + C_{N_{\text{ji}}}\right) \tag{12}$$

If the jet nozzle is properly characterized, the jet force can be calculated directly in the following:

$$C_{N_j} = \frac{[(1+\gamma)/\gamma]\dot{m}u_e - p_\infty A_e}{\tfrac{1}{2}\rho_\infty a_\infty^2 M^2 S_{\text{ref}}} \tag{13}$$

Such characterization has been performed in the wind-tunnel tests and is a necessary prerequisite for determining the boundary conditions for the jet as modeled in the computational fluid dynamics (CFD) computations.

The relative magnitudes of the jet force and the jet-interaction force can be compared through a jet-interaction amplification factor K, as shown in Eq. (14):

$$K = (F_j + F_{\text{ij}})/F_j \tag{14}$$

An amplification factor greater than 1 indicates that the jet-interaction force amplifies or increases the total force produced by the jet, whereas an amplification factor less than 1 indicates that the jet-interaction force reduces the total force produced by the jet.

Figures 18 and 19 illustrate the relationship between the total force coefficient and its three components as a function of distance down the body. The total normal force shows an increase over the front part of the body caused by the lift produced by the AOA. Approximately 1 caliber in front of the jet, the total normal force begins to deviate from the no-jet normal force as a result of the interaction of the jet with the external flow. The total normal force shows a large decrease near the jet caused by the downward force produced by the jet. The total normal force increases gradually behind the jet because of the AOA and jet-interaction effects. Figure 19 shows the three components of the total force coefficients. For this particular case the jet-interaction force coefficient $C_{N_{\text{ji}}}$ is about 3% of the jet force coefficient C_{N_j} and acts in the opposite direction, resulting in an amplification factor of $K = 0.97$.

The effect of mass flow on the jet-interaction force is shown in Fig. 20. Over the forward 6.3 calibers of the body, a similar variation in the jet-interaction force is seen despite larger differences in mass flow (0.36 vs 0.54 kg/s). Over the rear two calibers of the body, the effect of mass flow on the jet-interaction force is more evident because of the effect of the recompression shock. As noted in the discussion of the pressure results, the recompression shock moves rearward as the mass-flow rate increases from 0.36 to 0.54 kg/s. The rearward movement of the recompression shock produces a small increase in the jet-interaction force. The jet force is more directly affected by the mass-flow rates as shown in Eq. (13). The results clearly show the complex dependence of the jet-interaction force on body length and mass-flow rate.

The jet-interaction force coefficient shows a strong dependence on Mach number for similar (dimensional) mass-flow rates between Mach 2 and 3.3, as shown in Fig. 21. At Mach 3.3 the jet-interaction force is only 3% of the jet force, whereas at Mach 2 the jet-interaction force is 20% of the jet force. In both cases the jet-interaction force opposes the jet force, resulting in a deamplification ($K = 0.97$ and 0.80 at Mach 3.3 and 2, respectively). As shown in Fig. 22, the longitudinal pressure distributions, particularly behind the jet, show very similar variations despite the differences in Mach number. All of the bodies in question have deamplification in the presence of the jet, except S4-1. Behind the jet there is a large low-pressure region, which extends down the body. This low-pressure region is primarily responsible for the deamplification. By shortening the body by one caliber (S4-1), there will be less deamplification because the length of the body over which this low-pressure region act is reduced.

These results cannot be directly extrapolated to free-flight conditions because there has been no scaling of the jet characteristics relative to the freestream conditions. The results do show, however,

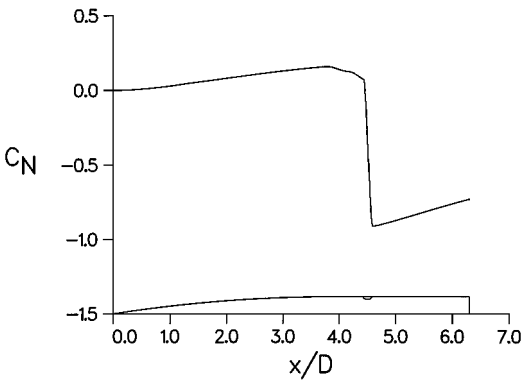

Fig. 18 Total normal force distribution over the body: 4-caliber ogive, $M = 3.3$, $\alpha = 4$ deg.

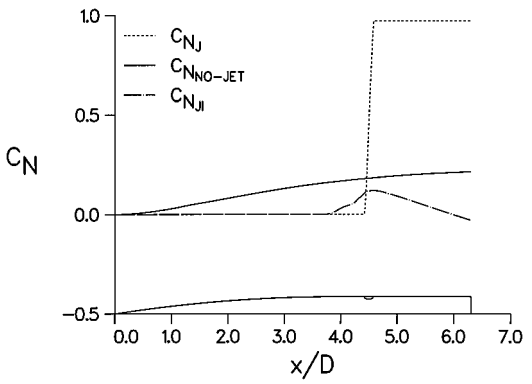

Fig. 19 Components of normal force distribution over the body: 4-caliber ogive, $M = 3.3$, $\alpha = 4$ deg.

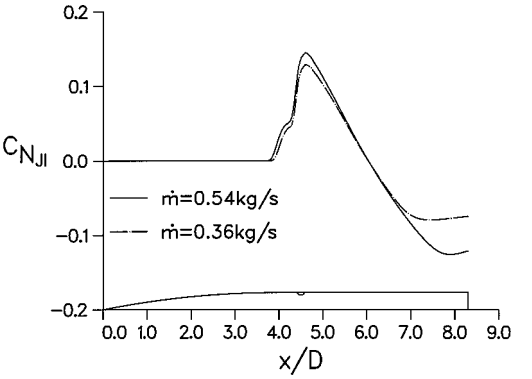

Fig. 20 Effect of mass flow on jet-interaction force: $M = 3.33$, 4-caliber sharp ogive.

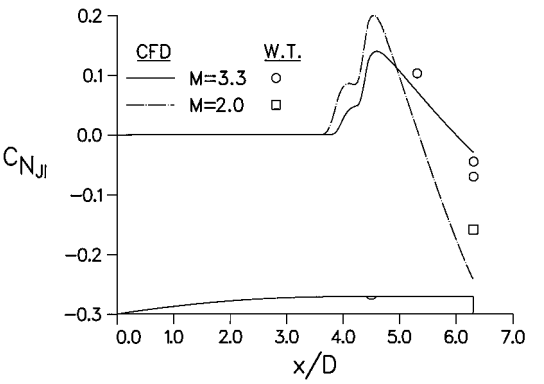

Fig. 21 Effect of Mach number on jet-interaction force: 4-caliber sharp ogive.

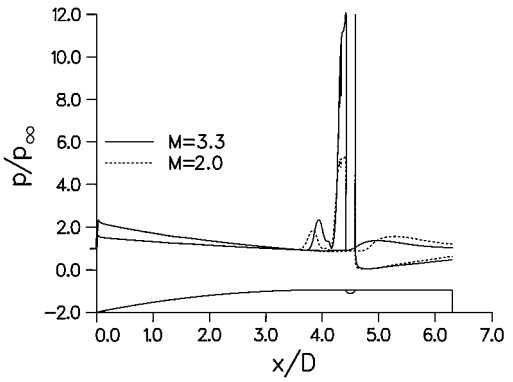

Fig. 22 Effect of Mach number on longitudinal pressure distribution: $\phi = 0$ and 180 deg.

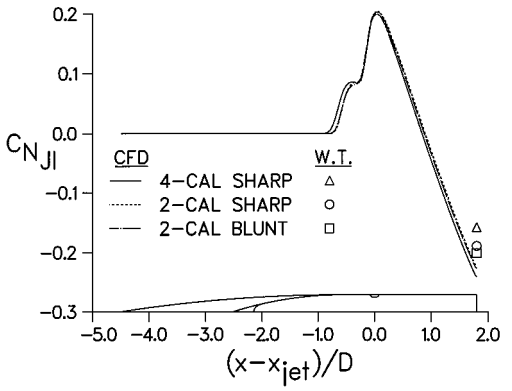

Fig. 23 Effect of nose shape on jet-interaction force: $M = 2.0$.

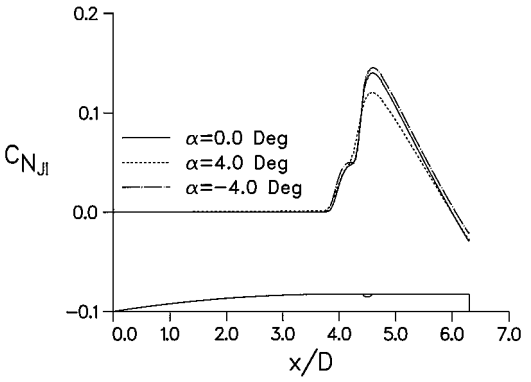

Fig. 24 Effect of AOA on jet-interaction force: $M = 3.3$, 4-caliber sharp ogive.

that the jet-interaction effects can be significant, and these effects can be accurately predicted by the computational method.

The effect of nose shape on the jet-interaction force and moment have also been considered in the wind-tunnel and computational investigations. Figure 23 shows the jet-interaction force for the three different nose shapes considered in the study. The 2-caliber blunt and sharp noses have nearly the same force variation over the body. The 4-caliber sharp ogive shows a slight variation from the 2-caliber ogive noses. The variation is likely caused by small differences in the body slope in the forward portion of the recirculation region in front of the jet. The body slope of the 4-caliber ogive is smaller allowing the recirculation region to extend farther forward than the 2-caliber ogive cases. Similar results were obtained for the jet-interaction moment.

The effect of AOA on the jet-interaction force is shown in Fig. 24 for the $L/D = 6.3$ 4-caliber ogive at Mach 3.3. Results were obtained for AOA of −4, 0, and 4 deg. All three AOA show nearly the same total jet-interaction force, although when the jet exit is on the lee side of the body ($\alpha = 4$ deg) the jet-interaction force

Table 1 Comparison of predicted and measured jet-interaction forces

Body type	Test no.	Mach no.	α, deg	C_{N_j}	$C_{N_{ji}}$ CFD	$C_{N_{ji}}$ W.T.
S4	23,645	3.3	0	1.070	−0.029	−0.07
S4	23,645	3.3	4	1.070	−0.028	−0.05
S4	23,645	3.3	−4	1.070	−0.021	−0.08
S4	23,662	3.3	0	1.045	−0.029	−0.045
S4-1	23,663	3.3	0	1.027	0.072	0.103
S4	23,644	2.0	0	1.188	−0.240	−0.158
S2	23,641	2.0	0	1.134	−0.223	−0.189
BL2	23,642	2.0	0	1.161	−0.227	−0.201

Table 2 Comparison of predicted and measured jet force amplification factor

Body type	Test no.	Mach no.	K CFD	K W.T.
S4	23,645	3.3	0.97	0.935
S4	23,662	3.3	0.97	0.96
S4-1	23,663	3.3	1.07	1.10
S4	23,644	2.0	0.80	0.87
S2	23,641	2.0	0.80	0.83
BL2	23,642	2.0	0.80	0.83

Table 3 Comparison of predicted and measured jet-interaction moment

Body type	Test no.	Mach no.	$C_{m_{ji}}$ CFD	$C_{m_{ji}}$ W.T.
S4	23,645	3.3	−0.202	−0.21
S4	23,662	3.3	−0.201	−0.20
S4-1	23,663	3.3	−0.069	−0.09
S4	23,644	2.0	−0.481	−0.46
S2	23,641	2.0	−0.469	−0.46
BL2	23,642	2.0	−0.468	−0.44

appears to show slightly more variation in the vicinity of the jet. Larger variations in the jet-interaction force with AOA were noted for the $L/D = 8.3$, 4-caliber ogive. These variations were produced by the rearward movement of the recompression shock for positive AOA and forward movement of recompression shock at negative AOA. The effect of the recompression shock on the jet-interaction force over the rear two caliber of the $L/D = 8.3$, 4-caliber ogive at $\alpha = 0$ deg was shown in Fig. 20. The effect of the recompression shock was not evident for the shorter $L/D = 6.3$ body. Similar variations in the location of the recompression shock were noted in the wind-tunnel pressure tests, although no force and moment measurements were obtained for the longer body.

Comparison with Wind-Tunnel Global Measurements

Tables 1–3 show the comparisons of the forces, amplification factors, and moments with wind-tunnel measurements. The four bodies are represented in the tables: the $L/D = 6.3$ body with a 4-caliber sharp-nose ogive (S4), the $L/D = 5.3$ body with a 4-caliber sharp-nose ogive (S4-1), the $L/D = 4.3$ body with a 2-caliber sharp-nose ogive (S2), and the $L/D = 3.94$ body with a 4-caliber blunt-nose ogive (BL2). The comparisons show that the CFD predictions appear to slightly underpredict the jet-interaction force at Mach 3.3 and slightly overpredict the jet-interaction force at Mach 2, with the force amplification factor generally predicted to within about 3%. The computed and measured moments were referenced to the center of the jet exit, eliminating the jet thrust as contributor to the moment. Thus, the moment is caused purely by the jet-interaction effect. The predicted moments are believed to be within the experimental error.

Conclusions

A computational approach has been validated with experimental data for axisymmetric bodies with lateral jet in supersonic flight at low AOA. The surface-pressure comparisons generally are in good

agreement with previously published experimental results. The presence of the jet produces a complex flowfield, which is characterized by a high-pressure region upstream of the jet and a low-pressure region downstream.

The total force acting on the projectile caused by the jet consists of two components: the pressure and momentum flux at the nozzle, and the interaction of the jet with the external flowfield. The focus of the current study is on the jet interaction with the external flowfield and assumes that the nozzle flow and resulting force and moment associated with the nozzle have been fully characterized. For the cases examined here, the jet-interaction portion is smaller than the force produced by the jet, but still is a significant factor in the total force. Comparison between the predicted jet-interaction force and moment and wind-tunnel measurements are typically within the experimental accuracy. Both the computations and experiment show that Mach number, body length, and mass flow appear to have the most significant effect on the jet-interaction force. For the bodies examined here, nose shape and small variation in AOA appeared to have little effect on jet-interaction force and moment, although the predictions indicate that AOA effects may be more important in longer bodies.

The predicted results show some discrepancy with the experimental measurements in the vicinity of the recirculation region in front of the jet and at the end of the body near the recompression shock although effect on the global forces and moments appears to be small. Potentially, these shortcomings can be addressed with more accurate turbulence modeling. Despite these shortcomings, the computational approach does appear to adequately capture the main features of the complex flow and is expected to yield accurate global force and moment predictions.

Acknowledgments

The experimental data that formed the basis for the computational validation were provided courtesy of RAFAEL, Israel Ministry of Defense Directorate of Defense Research and Development. Computational resources were obtained through a grant of computer time from the Army Research Laboratory Major Shared Resource Center through the U.S. Department of Defense High Performance Computing (HPC) Modernization Program. Additionally, support for the development and parallelization of the ZnsFlow code has been made through the Department of Defense HPC Modernization CHSSI program.

References

[1]Brandeis, J., and Gill, J., "Experimental Investigation of Super- and Hypersonic Jet Interaction on Missile Configurations," *Journal of Spacecraft and Rockets*, Vol. 35, No. 3, 1998, pp. 296–302.

[2]Brandeis, J., and Gill, J., "Experimental Investigation of Side-Jet Steering for Supersonic and Hypersonic Missiles," *Journal of Spacecraft and Rockets*, Vol. 33, No. 3, 1996, pp. 346–352.

[3]Spaid, F. W., and Zukoski, E. E., "A Study of the Interaction of Gaseous Jets from Transverse Slots with Supersonic External Flows," *AIAA Journal*, Vol. 6, No. 2, 1968, pp. 205–212.

[4]Gilman, R. G., "Control Jet Interaction Investigation," *Journal of Spacecraft and Rockets*, Vol. 8, No. 4, 1971, pp. 334–339.

[5]Spaid, F. W., "Two-Dimensional Jet Interaction Studies at Large Values of Reynolds and Mach Numbers," *AIAA Journal*, Vol. 13, No. 11, 1975, pp. 1430–1434.

[6]McMaster, D. L., Shang, J. S., and Golbitz, W. C., "Supersonic, Transverse Jet from a Rotating Ogive Cylinder in a Hypersonic Flow," *Journal of Spacecraft and Rockets*, Vol. 26, No. 1, 1989, pp. 24–30.

[7]Chamberlain, R., "Calculation of Three-Dimensional Jet Interaction Flowfields," AIAA Paper 90-2099, July 1990.

[8]Hsieh, T., and Wardlaw, A. B., "Numerical Simulation of Cross Jets in Hypersonic Flow Over a Biconic Body," AIAA Paper 94-0165, Jan. 1994.

[9]Sahu, J., "Numerical Computations of Three-Dimensional Jet Interaction Flow Fields," AIAA Paper 94-3521, Aug. 1994.

[10]Srivastava, B., "Aerodynamic Performance of Supersonic Missile Body- and Wing Tip-Mounted Lateral Jets," *Journal of Spacecraft and Rockets*, Vol. 35, No. 3, 1998, pp. 278–286.

[11]Baldwin, B. S., and Lomax, H., "Thin Layer Approximation and Algebraic Model for Separated Turbulent Flows," AIAA Paper 78-257, Jan. 1978.

[12]Cebeci, T., "Calculation of Compressible Turbulent Boundary Layers with Heat and Mass Transfer," AIAA Paper 70-741, June–July 1970.

[13]Ying, S. X., Steger, J. L., Schiff, L. B., and Baganoff, D., "Numerical Simulation of Unsteady, Viscous, High-Angle-of-Attack Flows Using a Partially Flux-Split Algorithm," AIAA Paper 86-2179, Aug. 1986.

[14]Sahu, J., and Steger, J. L., "Numerical Simulation of Three-Dimensional Transonic Flows," *International Journal for Numerical Methods in Fluids*, Vol. 10, 1990, pp. 855–873.

[15]Steger, J. L., and Warming, R. F., "Flux Vector Splitting of the Inviscid Gasdynamic Equations with Application to Finite-Difference Methods," *Journal of Computational Physics*, Vol. 40, April 1981, pp. 263–293.

[16]Steger, J. L., and Buning, P., "Developments in the Simulation of Compressible Inviscid and Viscous Flow on Supercomputers," NASA TM 86674, 1985.

[17]Beam, R., and Warming, R. F., "An Implicit Factored Scheme for the Compressible Navier–Stokes Equations," *AIAA Journal*, Vol. 16, No. 4, 1978, pp. 393–402.

[18]Benek, J. A., Donegan, T. L., and Suhs, N. E., "Extended Chimera Grid Embedding Scheme with Application to Viscous Flows," AIAA Paper 87-1126, June 1987.

[19]Pulliam, T. H., and Steger, J. L., "On Implicit Finite-Difference Simulations of Three-Dimensional Flow," *AIAA Journal*, Vol. 18, No. 2, 1982, pp. 159–167.

R. M. Cummings
Associate Editor